Astrocytes in the mouse brain respond bilaterally to unilateral retinal neurodegeneration

Melissa L. Cooper[a],[1] (iD), Holly K. Gildea[a], Maria Clara Selles[a], Eleni Katafygiotou[a], Shane A. Liddelow[a,b,c] (iD), and Moses V. Chao[a,b,d,1] (iD)

Affiliations are included on p. 9.

Glaucomatous optic neuropathy, or glaucoma, is the world's primary cause of irreversible blindness. Glaucoma is comorbid with other neurodegenerative diseases, but how it might impact the environment of the full central nervous system to increase neurodegenerative vulnerability is unknown. Two neurodegenerative events occur early in the optic nerve, the structural link between the retina and brain: loss of anterograde transport in retinal ganglion cell (RGC) axons and early alterations in astrocyte structure and function. Here, we used whole-mount tissue clearing of full mouse brains to image RGC anterograde transport function and astrocyte responses across retinorecipient regions early in a unilateral microbead occlusion model of glaucoma. Using light sheet imaging, we found that RGC projections terminating specifically in the accessory optic tract are the first to lose transport function. Although degeneration was induced in one retina, astrocytes in both brain hemispheres responded to transport loss in a retinotopic pattern that mirrored the degenerating RGCs. A subpopulation of these astrocytes in contact with large descending blood vessels were immunopositive for LCN2, a marker associated with astrocyte reactivity. Together, these data suggest that even early stages of unilateral glaucoma have broad impacts on the health of astrocytes across both hemispheres of the brain, implying a glial mechanism behind neurodegenerative comorbidity in glaucoma.

astrocyte | glaucoma | neurodegeneration | reactivity | visual system

Glaucoma is a neurodegenerative disease impacting vision in 80 million people worldwide, a number projected to increase as the world's population ages (1). Elevated intraocular pressure (IOP) is the only known modifiable risk factor for glaucoma (2, 3) and is one of the main indicators used for its clinical diagnosis (4). Despite its clinical ubiquity, IOP elevation is not an accurate indicator of the disease. Over 90% of individuals diagnosed with ocular hypertension do not develop glaucoma in the subsequent 15 y (5), while many others with IOP within the normal range do (6). Glaucoma's incomplete etiology means that we need to understand the factors influencing susceptibility in the nervous system tissues that actually degenerate: the retina, optic nerve, and downstream visual pathways. Further, there is evidence of comorbidity between glaucoma and several other neurodegenerative conditions across the central nervous system, such as stroke and Alzheimer's Disease (7–10), but the links between neurodegeneration in the eye and neurodegenerative vulnerability in the brain are unknown. Understanding the earliest events in disease progression is critical for earlier diagnoses and provides the best opportunity to prevent vision loss in impacted individuals or implement neuroprotective therapies (11). It also provides insight into general neurodegenerative progression that will help us understand events that increase one's susceptibility to neurodegeneration.

In glaucoma, two neurodegenerative events occur early in the optic nerve, the structural link between retina and brain: loss of anterograde transport in retinal ganglion cell (RGC) axons (12, 13) and early alterations in astrocyte structure and function (14–17). Without intact transport, mitochondrial mobilization from the RGC body to the distal axon is impaired, lowering the threshold for metabolic stress (13, 18, 19). Early astrocyte responses are thought to have a positive impact on progression of glaucoma pathology. Recent work has shown that unilateral IOP elevation results in early, bilateral alterations in astrocytes within the retina and optic nerves (14, 15, 17, 20–23). Morphological, metabolic, inflammatory, and gap junction coupling changes have all been reported across both optic nerves even when IOP is elevated unilaterally (20–22), and manipulating these responses can dramatically alter the time course of degeneration (15). While retinal and optic nerve glia have been examined in the context of IOP elevation, many of the earliest known neurodegenerative events in glaucoma occur in distal RGC axons in the brain (12, 19). The way astrocytes in the brain respond to these events is unknown. It has long been thought that changes in astrocytes may predict neuronal degeneration. Knowing how to predict

Significance

Glaucoma is comorbid with many neurodegenerative diseases, but links between retinal and brain neurodegeneration are unknown. In the optic nerve, the structural link between retina and brain, the earliest known neurodegenerative events in glaucoma are 1) loss of anterograde transport function in retinal ganglion cell (RGC) axons and 2) changes to astrocyte structure and function. Here, we cleared full mouse brains after inducing a unilateral glaucoma model to see how these neurodegenerative events impact the brain. We found that RGC axons terminating in specific brain regions degenerate first, independent of axonal length. We also found that unilateral retinal neurodegeneration causes bilateral astrocyte responses in the brain itself. Those responses occur in a retinotopic pattern that mirrors that of degenerating RGCs.

[1]To whom correspondence may be addressed. Email: melissa.cooper@nyulangone.org or moses.chao@nyulangone.org.

degeneration by studying early changes in astrocytes may eventually help us prevent neuronal loss.

In this study, we used an iDISCO-based (24) clearing method to image RGC anterograde transport across the intact optic projection 1 wk after unilateral IOP elevation via the microbead occlusion model (MOM). Using light sheet imaging of intact brains, we compare patterns of RGC degeneration in retinorecipient regions in relation to astrocyte responses. We found that RGC projections terminating in specific contralateral retinorecipient targets lose anterograde transport capacity at this early neurodegenerative stage. Analyses of glial fibrillary acidic protein (GFAP) immunoreactivity suggest that astrocytes in both hemispheres of the brain are responsive to unilateral IOP elevation, even before complete loss of axonal transport. A subpopulation of these astrocytes in contact with large descending blood vessels are labeled by a marker frequently associated with astrocyte reactivity, lipocalin-2 (LCN2) (25), suggesting an interaction between local unilateral degenerative patterns and bilateral induction of astrocyte responses.

Results

RGC Anterograde Transport Efficiency Does Not Depend on Axonal Length.
We began by mapping the visual projection's capacity for anterograde axonal transport across retinorecipient targets using cholera toxin beta (CTB) tracing (12). CTB injected into the posterior chamber of the eye (Fig. 1A) was taken up by RGCs and transported anterograde through their axons into their termini in the brain (Fig. 1B). Combining this method with tissue clearing and lightsheet microscopy (Fig. 1C) allowed us to quantify RGC anterograde transport in fully transparent, whole brains. Images were rendered in three-dimensions to be analyzed as a complete visual pathway (Fig. 1 D and E). Using Imaris image analysis software, visual projections were segmented into contralateral and ipsilateral streams (Fig. 1F), then further segmented by retinorecipient target (Fig. 1G). We then quantified the tissue volume with positive CTB fluorescence in the full projection, ipsilateral and contralateral projections, and each region containing RGC termini (Fig. 1H). For each of these regions, we also examined the mean CTB intensity values, indicating the anterograde transport efficiency for RGCs projecting to different parts of the visual stream within the same brain. We then compared these values to the mean values across the full visual projections (Fig. 1I).

While transport efficiency was relatively uniform across RGCs projecting to ipsilateral brain regions, RGCs projecting to contralateral regions exhibited different transport efficiencies depending on their retinorecipient target. RGCs projecting to the cOPN exhibited a particularly high level of anterograde transport, followed by the cLGN and cSC. Although they terminate in the closest region to the retina and thus have the shortest distance to transport CTB, axons projecting to the SCN had a significantly lower transport efficiency than the average of all RGCs. Axonal length, therefore, was not the primary factor determining transport efficiency. Instead, RGC subtypes projecting to different retinorecipient targets exhibit varied capacity for anterograde axonal transport.

Anterograde Transport in the Contralateral Optic Projection Slows in Early Neurodegeneration.
Next, we compared anterograde transport in brains in early stages of glaucomatous neurodegeneration to that of sham controls (Fig. 2 A and B). To unilaterally elevate IOP, we intracamerally injected five mice with microbeads in one eye; five additional mice received unilateral sham injections as control. IOP was monitored bilaterally for 5 d, until CTB was injected into the microbead or sham eye (Fig. 2C).

IOP in microbead-injected eyes elevated from 14.3 ± 0.7 mmHg preinjection to 20.4 ± 1.1 mmHg postinjection; contralateral eyes and both eyes in control mice did not exhibit an IOP elevation.

Only the accessory optic tract (AOT), a distal midbrain retinorecipient target associated with the optokinetic response, showed a significant loss of CTB-containing tissue volume at this time point (Fig. 2D). However, when transport efficiency was assessed, contralateral superior colliculus (cSC), contralateral lateral geniculate nucleus (cLGN), contralateral olivary pretectal nucleus (cOPN), and AOT all showed a significant decrease following IOP elevation (Fig. 2E; isolated 3D renderings of each region in Fig. 2 G–L). AOT is a region uniquely containing contralateral RGC projections, meaning that each retinorecipient target with a deficit in anterograde transport function was on the contralateral side of the brain. We did not detect a change in ipsilateral projection anterograde transport function.

Astrocytes Beyond the Retina and Optic Nerves Respond Retinotopically and Bilaterally to Unilateral IOP Elevation.
Even when RGC degeneration is unilateral, astrocytes in both retinas and optic nerves are known to respond to IOP elevation in one eye (15, 20, 21). To see whether astrocytes respond in the brain beyond the retina and optic nerves, we rehydrated the cleared brains and stained them to GFAP fluorescence across the same optic tracts as in Figs. 1 and 2. We focused on the three retinorecipient targets that showed the greatest change in mean fluorescence intensity (SC, LGN, and AOT) in the three brains that exhibited the greatest degree of degeneration in this initial examination. This allowed us to study astrocyte responses across the full optic tract and internally compare GFAP immunoreactivity patterns across portions of the same retinorecipient target with intact or dysfunctional transport.

In the degenerating tract's SC (Fig. 3 A–D) and LGN (Fig. 3 E and H), GFAP fluorescence was significantly higher in the portion of each region where transport had been lost compared to the portion of the same region with intact transport. The retinotopic pattern of GFAP fluorescence specific to each sample was mirrored in the opposite hemisphere, even though IOP was never elevated in the corresponding eye and RGC anterograde function was not impacted in the corresponding (ipsilateral) visual stream. This was true even though the pattern of RGC transport loss was different in all three brains; portions of SC or LGN with intact transport always had significantly less GFAP fluorescence than portions of the same brain regions with impaired transport, and the pattern in each brain reflected bilaterally.

AOT, however, showed the opposite pattern of GFAP fluorescence (Fig. 3 I–L). GFAP fluorescence was greatest within the portion of AOT with intact transport, and significantly lower in the portion that had lost transport. This pattern also occurred in the contralateral hemisphere's AOT. This may indicate that astrocytes in different visual system regions, or regions in different stages of degeneration, respond heterogeneously to IOP elevation independent of their distance from the retina, as SC and AOT reside in roughly the same coronal plane.

Astrocytes in the Midbrain React Bilaterally When RGCs Degenerate Unilaterally.
GFAP has previously been used as a stand-alone measure of astrocyte reactivity; however, GFAP levels are variable across brain regions at baseline and increases in GFAP immunoreactivity can reflect multiple, divergent reactive phenotypes (26–28). In addition, there are many studies showing profound astrocyte reactivity without changes in GFAP/Gfap levels (29, 30). To more closely examine astrocyte reactivity by immunostaining, we used LCN2, which is elevated in all reactive astrocyte subtypes reported thus far but not observed in astrocytes under baseline, healthy conditions (26, 31, 32).
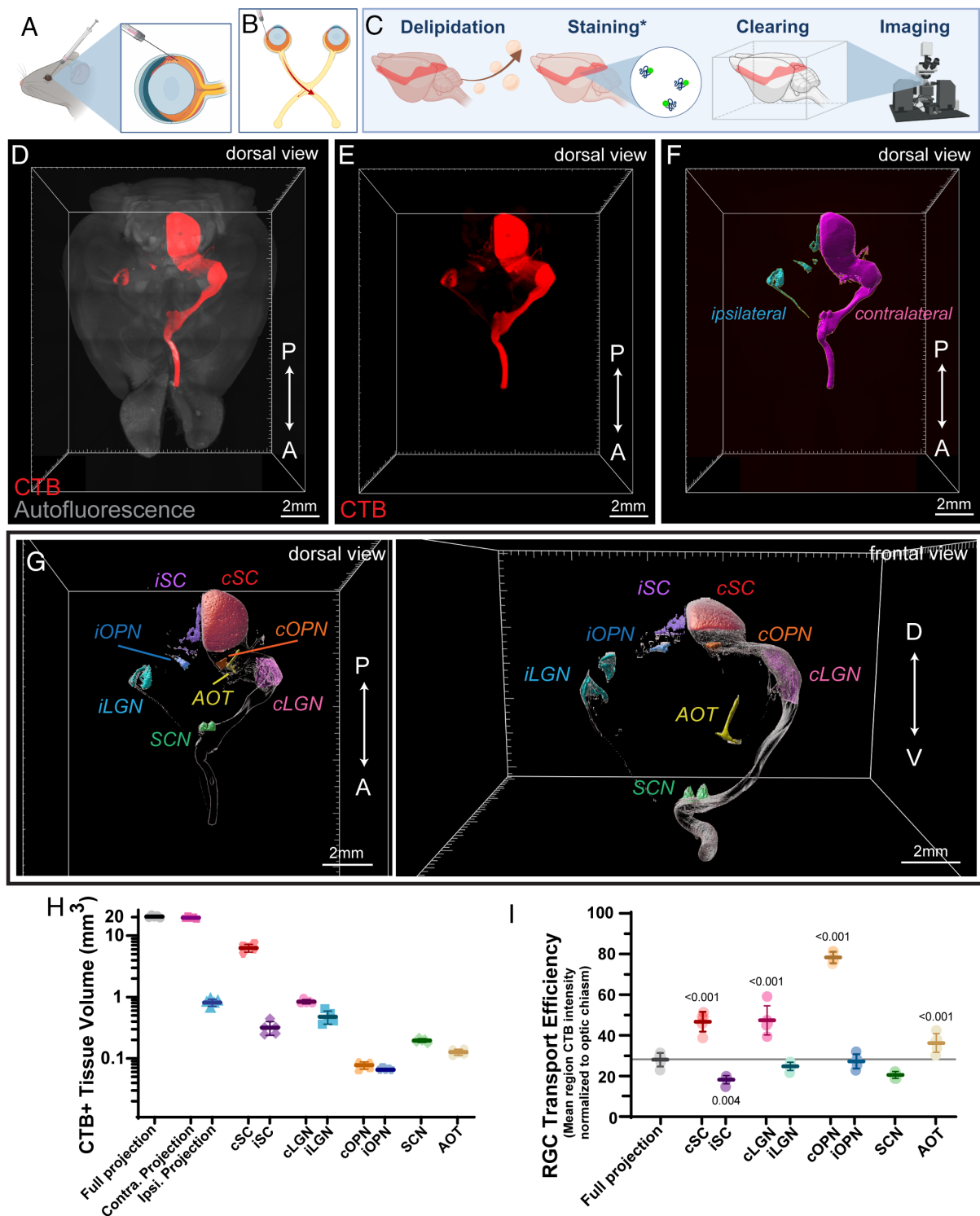
Fig. 1. RGC transport efficiency varies across the homeostatic optic projection. (*A*) CTB conjugated to AlexaFluor-555 was injected into the posterior chamber of the eye. (*B*) Following injection, CTB is transported anterograde to the brain. (*C*) Fixed brains (n = 5) were delipidated, then rehydrated and stained (as needed) before clearing and imaging on a light sheet microscope. (*D*) Dorsal view of the CTB (red) imaged within the entire optic projection in a cleared naïve adult (3-mo-old) mouse brain (white indicates full brain autofluorescence obtained in the 488 channel). A = anterior, P = posterior. (*E*) Dorsal view of the optic projection labeled with CTB, with optic nerve, lateral geniculate nucleus (LGN) superior colliculus (SC), and ipsilateral projection indicated. (*F*) The contralateral (magenta) and ipsilateral (cyan) optic projections were segmented from the image for quantification using Imaris. (*G*) Individual brain regions were also segmented; suprachiasmatic nucleus (SCN, green), contralateral LGN (cLGN, pink), contralateral olivary pretectal nucleus (cOPN, orange), contralateral SC (cSC, red), ipsilateral LGN (iLGN, cyan), ipsilateral OPN (iOPN, blue), and ipsilateral SC (iSC, purple) are all visible from the dorsal view (*Left*). The frontal view (*Right*) also shows the accessory optic tract (AOT, yellow) D = dorsal, V = ventral. (*H*) CTB-positive tissue volume within each analyzed brain region. (*I*) Mean CTB fluorescence intensity quantified across the full optic projection, normalized to the optic chiasm, and compared to that within individual brain regions as an indicator of RGC anterograde transport efficiency. Regions with CTB intensity significantly different from the average of the full homeostatic projection indicated with *P* values (determined via repeated measures one-way ANOVA followed by Tukey's test). *A*–*C* created with Biorender.com.
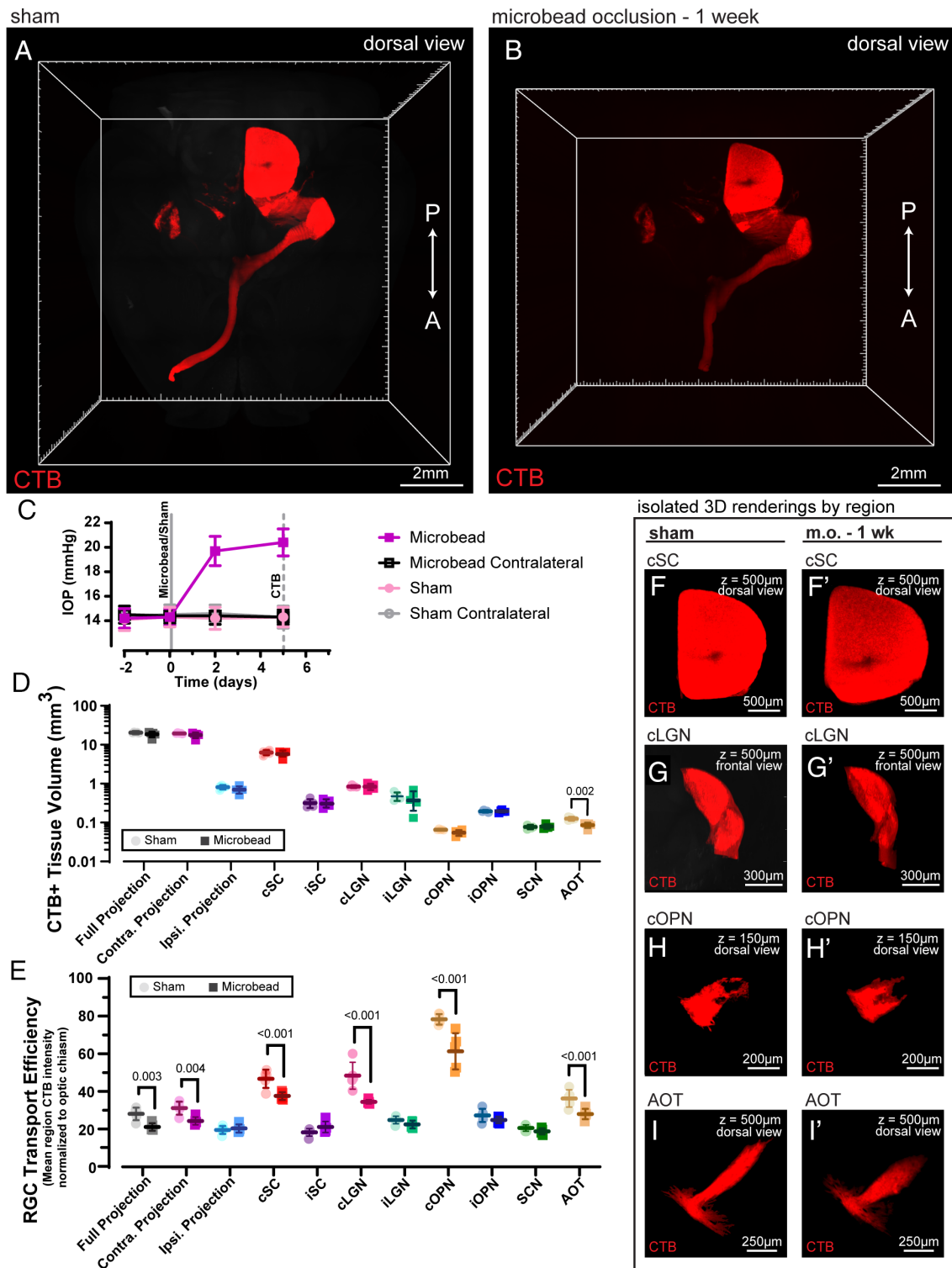
Fig. 2. Anterograde transport loss begins in specific RGC projections within the contralateral optic tract. (*A* and *B*) Dorsal views of complete, CTB labeled optic projections corresponding to sham or microbead-injected, IOP-elevated eyes in distinct mice. (*C*) IOP in all eyes measured via rebound tonometry. Anterior chamber microbead injection resulted in significant IOP increase over contralateral eye and sham condition. (*D*) Quantification of CTB+ tissue volume for each projection or in defined brain regions (n = 5 sham, n = 5 microbead). In each, sham (lighter circles on the left of each comparison) and microbead (darker squares on the right) are compared. There was a significant decrease in CTB labeling following IOP elevation in the AOT when compared to sham. (*E*) Differences in mean intensity (normalized to optic chiasm) across projection regions indicate more widespread deficits in RGC anterograde transport efficiency, particularly in the contralateral tract. The full projection exhibits significant change in CTB fluorescence (gray), but when divided into contralateral and ipsilateral projections (Fig. 1*F*) only the contralateral projection shows a significant change. This reduction in mean and median intensity in the contralateral projection is significant in SC (*F* and *F′*), LGN (*G* and *G′*), and OPN (*H* and *H′*) as well as the AOT (*I* and *I′*). Significance for *D* and *E* determined via two-way ANOVA followed by Tukey's test to compare sham and microbead values in each region analyzed. Adjusted *P* values for each significant (α ≤ 0.05) comparison indicated on graphs.
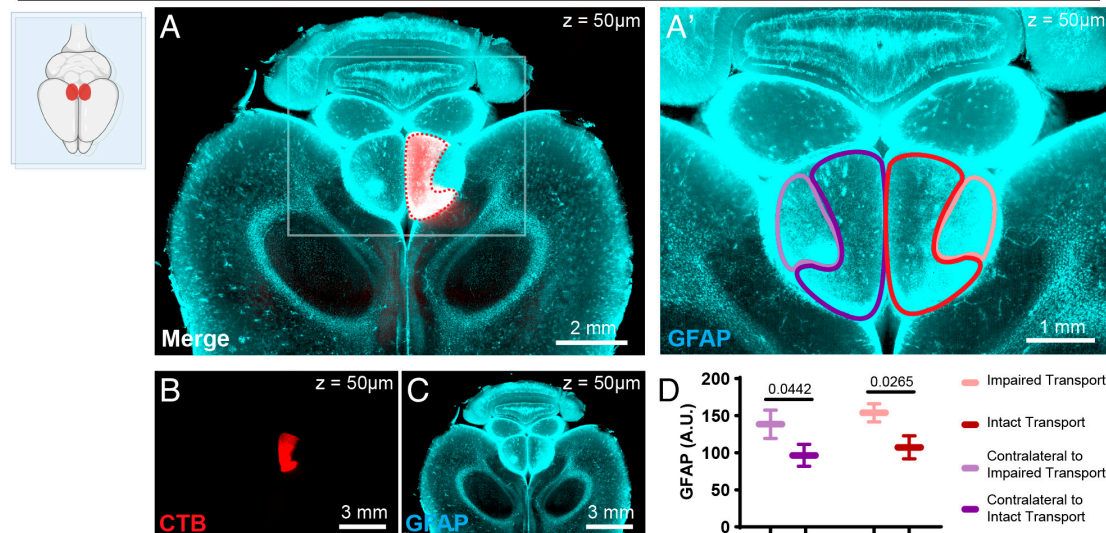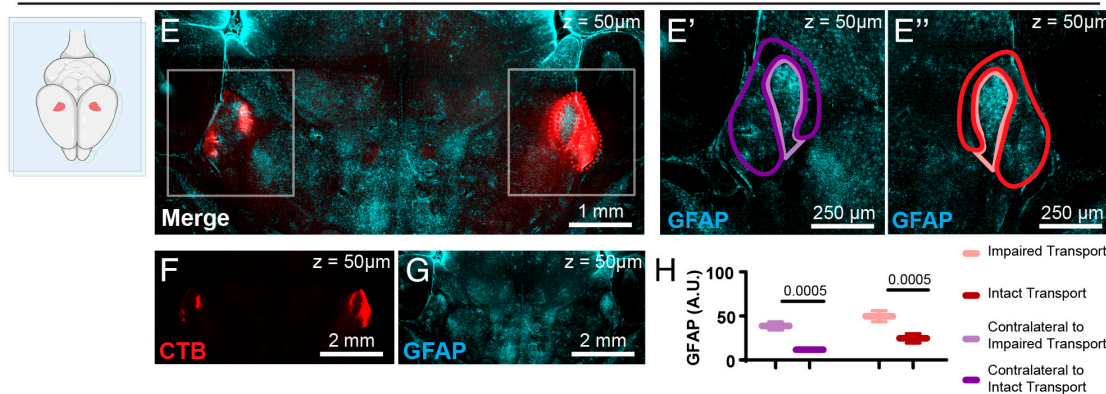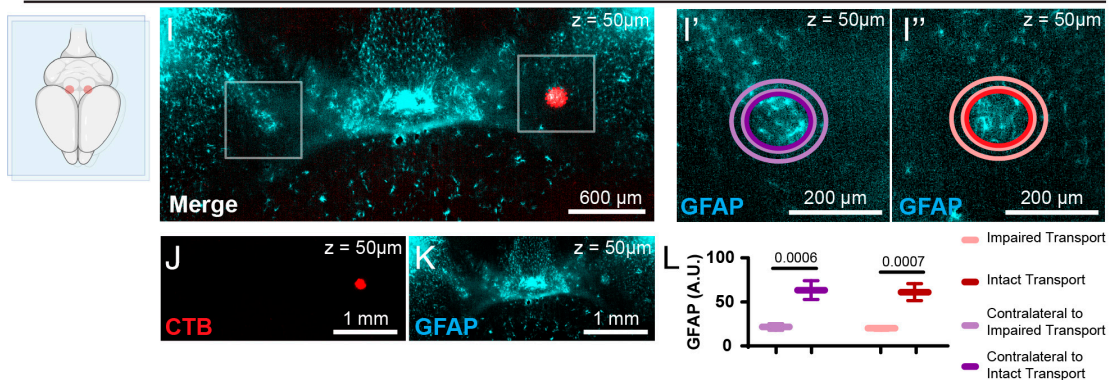
Fig. 3. Astrocyte responses across visual brain regions bilaterally and retinotopically mirror unilateral RGC degenerative patterns. Brains (n = 3) were rehydrated and restained for GFAP to examine astrocyte cytoskeletal elements in degenerating visual streams. (*A*) Virtual slice in horizontal plane containing SC [merge of CTB (red, *B*) and GFAP (cyan, *C*)]. (*D*) GFAP fluorescence intensity in tissue with intact anterograde transport (red outline) is significantly lower than GFAP fluorescence intensity in the portion of SC with impaired anterograde transport (pink). Tissue contralateral to and retinotopically matching these regions (purple, lavender) exhibits the same pattern of GFAP intensity. This also occurred in LGN (*E–H*), while the AOT (*I–L*) exhibited the opposite pattern of GFAP intensity relative to RGC transport impairment. Significance for *D*, *H*, and *I* determined by one-way ANOVA followed by Tukey's test. Adjusted *P* values for each significant (α ≤ 0.05) comparison indicated on the graph. Blue diagrams showing brain region locations were generated with Biorender.com.

We rehydrated, sectioned, and restained our samples to compare RGC anterograde transport (Fig. 4 *A* and *E*) and patterns of GFAP immunoreactivity (Fig. 4 *B* and *F*) to LCN2 immunopositivity in the SC, the primary retinorecipient target in the mouse brain and one of the most distant regions from the retina itself (33). As previously reported (26, 32), we did not detect LCN2

labeling within astrocytes in sham brains (Fig. 4 *C* and *I*, *Inset*). In regions with impaired transport following IOP elevation, we found that a subset of GFAP+ astrocytes in direct contact with descending vasculature were labeled by LCN2. This response occurred bilaterally (Fig. 4 *G*, *J*, and *K*, *Insets*). When quantified, LCN2 signal was bilaterally elevated in microbead brains
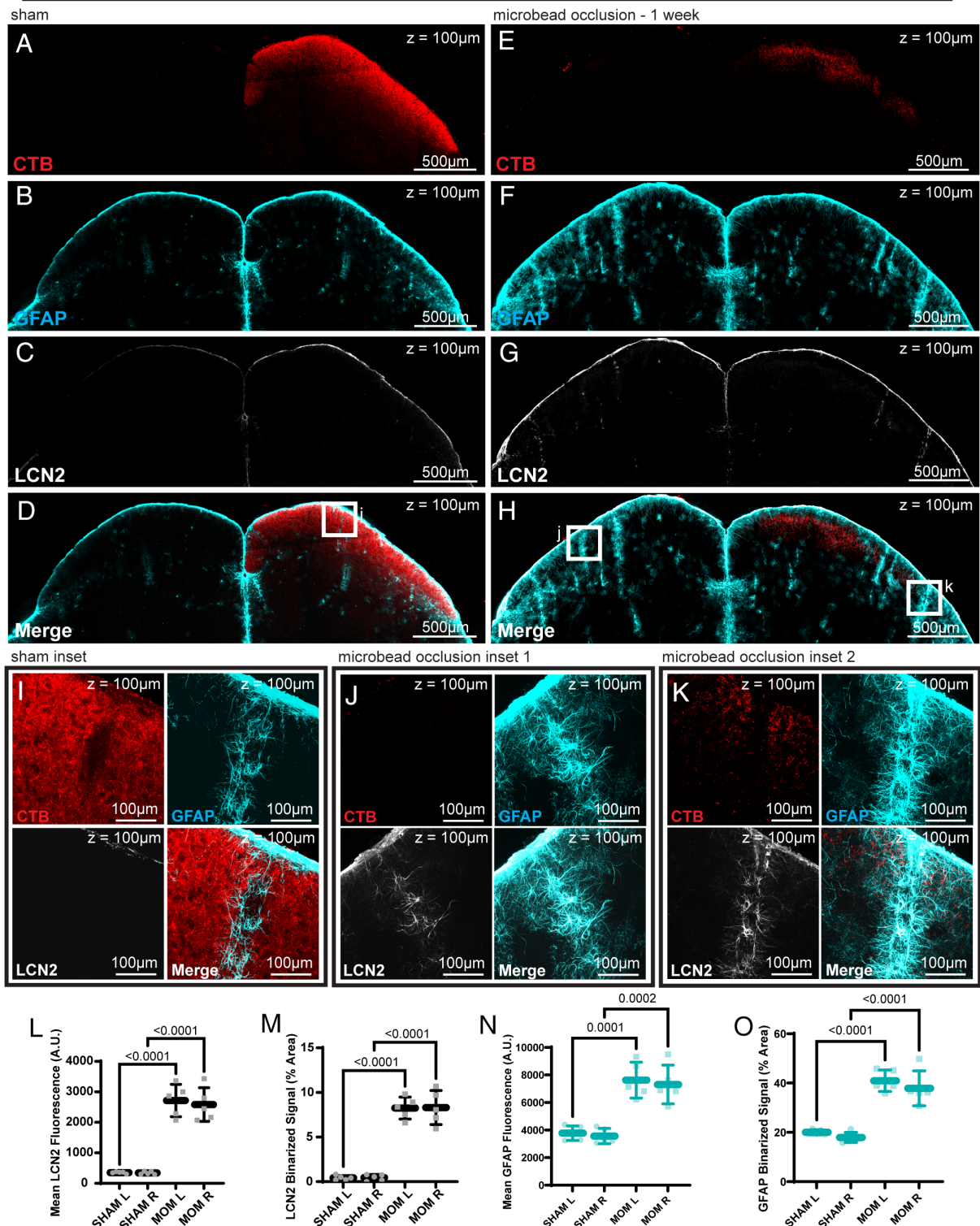
Fig. 4. Bilateral astrocyte responses include reactive astrocytes. Tissue sections from sham (*A–D*; n = 5) and microbead occlusion (*E–H*; n = 5) samples, imaged for CTB (red), GFAP, (cyan), and LCN2 (white) immunopositivity. (*I*) Higher-resolution *Inset* from sham sample indicating immunopositivity around descending vasculature. GFAP is detected surrounding vasculature but not lipocalin-2 (LCN2). (*J* and *K*) Ipsilateral and cSC insets corresponding to unilateral microbead occlusion condition. GFAP and LCN2 are detected around descending blood vessels on both sides of the brain. (*L*) Mean LCN2 fluorescence was significantly upregulated in bilateral SCs when IOP was unilaterally increased; the same was true of (*M*) the percentage of SC positive for LCN2 signal. There was no significant difference in LCN2 levels between hemispheres in either condition. (*N* and *O*) Like LCN2, GFAP is significantly bilaterally upregulated in the unilateral microbead occlusion condition relative to sham when measured by mean fluorescence and binarized signal. Significance was determined by one-way ANOVA followed by Tukey's test. Adjusted *P* values for each significant (α ≤ 0.05) comparison between hemispheres [right (R) and left (L)] in the same brain or the same hemisphere in sham/MOM indicated on the graph. MOM = microbead occlusion model.

compared to sham, and LCN2 reactivity did not differ between hemispheres in the same brains (Fig. 4 *L* and *M*). This pattern also occurred for GFAP (Fig. 4 *N* and *O*). Taken together, these data indicate that astrocytes respond bilaterally to unilateral IOP elevation, even when neurons do not exhibit bilateral signs of degeneration.

Discussion

Here, we use an unbiased approach to assess visual system anterograde transport impairments following unilateral IOP elevation across whole, cleared brains. We identified that the AOT exhibits significant degeneration prior to any other retinorecipient target. The AOT is a retinotopically organized region containing projections from direction-selective RGCs (dsRGCs). The AOT is responsible for the horizontal optokinetic reflex, a reflex often tested in mouse models of glaucoma but not yet clinically utilized for disease detection. Mice with elevated IOP have been repeatedly shown to exhibit significant, early deficits in optokinetic reflex induction typically associated with altered spatial resolution capacity (15, 34, 35); however, we find that the region responsible for inducing the reflex itself may be impaired first by elevated IOP, prior to degeneration in the primary visual pathway responsible for conscious vision. Thus, rather than testing spatial resolution, the field may have been assessing degeneration in the AOT when testing the optokinetic reflex. Optokinetic reflex assessments are not currently used when diagnosing glaucoma in clinical settings. If human glaucomatous progression follows the same pattern as mouse anterograde transport loss, our data indicate that clinically implementing optokinetic reflex assessments could be an efficient and effective measure of the earliest stages of RGC dysfunction following IOP elevation.

Even in homeostatic brains, anterograde transport capacity differs among RGCs projecting to different retinorecipient targets. Axonal length was not an indicator of the amount of CTB transport along an axon to its terminus; in fact, axons terminating in the SCN, the closest RGC terminal region to the retina, exhibit significantly less CTB transport than the average RGC. Interestingly, retinorecipient targets containing axons that exhibited the greatest anterograde transport capacity were also the first to show a significant impairment following IOP elevation. While changes in regions that initially exhibit greater-magnitude values may be easier to detect, particular RGC subtypes, especially those with dendrites in the off sublamina, are still known to be more susceptible to degeneration following IOP elevation (34, 36–38). Further, direction-selective RGCs (dsRGC), the RGC subtype that projects to the AOT (39), have been found to be particularly susceptible to both chronic (MOM and the genetic B6.*Sh3pxd2b*^*nee* model) and acute (optic nerve crush) degenerative stressors (40–42). Our data agree that dendritic stratification may not be the only differentiating factor among degenerating RGCs. RGCs with more robust anterograde transport demands may also be more susceptible to degeneration, in which case, there would be RGC subtype-specific vulnerability in both the dendritic and axonal compartments.

Both humans and mice have an AOT (39), but when comparing the species' full visual streams dsRGCs account for a greater proportion of mouse RGCs than primate (43, 44). This is because the majority of dsRGCs project to the SC, and the SC is the primary RGC target in the mouse visual system, a system adapted to prioritize movement detection (12, 33). Previous work indicates that dsRGCs are more susceptible to degeneration following IOP elevation than other RGC types (40, 42). Here, we find that the AOT degenerates prior to the SC, indicating that early-stage disease susceptibility can be further refined to subpopulations of

dsRGCs projecting to the AOT rather than SC. Additionally, while the dsRGC population as a proportion of the full projection greatly differs between primates and rodents, the proportion of RGCs projecting to the AOT is much more similar across species (33), and thus may be a more translatable finding.

Another difference among the mouse and primate visual systems is the number of ipsilateral- vs. contralateral-projecting RGC axons. Only about 5% of mouse RGCs project ipsilaterally (33), while in primates that number approaches 50% (45). While this difference may impact the unilaterality or bilaterality of RGC degeneration within the primate brain when compared to mouse, our data still show that bilateral astrocyte responses can be evoked by unilateral RGC degeneration—a phenomenon much clearer in a mammalian model with comparatively low binocular overlap.

By leaving the brain intact, we were able to detect retinotopic astrocyte responses that followed the pattern of transport loss or diminishment across multiple retinorecipient targets. Within the same SC or LGN, GFAP and/or LCN2 fluorescence were significantly higher in regions corresponding to diminished anterograde transport when compared to regions still containing RGC termini with fully intact transport. Importantly, the retinotopic pattern of GFAP upregulation was mirrored in the opposite hemisphere, which did not demonstrate any anterograde transport deficits in RGC axons originating in the degenerating retina. While still bilateral, the pattern of astrocyte responses changed in AOT. This may reflect a different response in the primarily white matter astrocytes within the AOT, or that the AOT is in a different degenerative phase than other brain regions even within the same brain. However, the astrocyte responses in each of these retinorecipient targets provide evidence that even when degeneration is local and unilateral, contralateral brain regions are not naïve to neurodegenerative stress, and glia are robustly responsive across the brain. Thus, scientists implementing internal controls should carefully consider how widespread astrocyte responses may alter the data they collect from brain regions contralateral to a neurodegenerative event.

It also indicates that astrocytes in the same brain region in opposite hemispheres may be communicating with one another. Previous work indicates that bilateral astrocyte responses preserve visual function by redistributing glycogen-derived metabolic resources from healthy to degenerating tissue through gap junctions (15). Astrocyte responses in the brain may serve a similar purpose. In the optic nerve, astrocyte-gap-junction-mediated metabolite transfer resulted in preservation of RGC transport function and the optokinetic response. The same mechanism in the brain could also preserve distal RGC axons. Yet, in the optic nerve, this protective response also made the donating tissue susceptible to further neurodegenerative stressors (15). If that is also the case in the brain, patients exhibiting glaucomatous neurodegeneration could be more susceptible to neurodegeneration in the brain itself. There is evidence of comorbidity and shared mechanisms among glaucoma and several neurodegenerative conditions, such as stroke and Alzheimer's Disease (7–10). Each of these diseases has different etiologies, so the common factor may be that astrocytes across the central nervous system have diminished capacity for metabolic redistribution following the initial stressor. Future experiments should examine gap junction connectivity among astrocytes in the central nervous system to determine potential susceptibilities in other CNS regions following IOP elevation, as well as which molecules are redistributed among astrocytes to better understand how the CNS supports degenerating tissue.

Another mechanism could involve the RGCs themselves. Higher-order visual system regions receiving bilateral inputs from the same retinotopic region may feed back signals to lower-order regions

(46) when those signals suddenly become unilateral; otherwise, there is evidence for a few retino-retinal axonal projections being maintained postnatally that could provide feed forward responses from lower-order regions (47). In this early stage of neurodegeneration, the significant bilateral responses are unlikely to be triggered solely by such feedback mechanisms in neurons. Yet, if neuronal feedback is involved, this would indicate that astrocytes are robustly responding to neuronal signals from a sequence of visual system regions that are not themselves degenerating, but merely receiving altered input signals from the higher- or lower-order regions they communicate with. If that were the case, that signal could represent an important initiator of an endogenously protective astrocyte response.

Human data indicates that during glaucomatous degeneration, visual fields lost in one visual stream are specifically preserved in the opposite visual stream such that a complete image is maintained across bilateral visual fields (48). While we did not see evidence of anterograde transport loss in ipsilateral projections, indicating that ipsilaterally projecting RGCs are largely undamaged at this early stage of degeneration, we still found bilateral astrocyte reactivity. This suggests a glial mechanism contributes to preservation of the full bilateral visual field. Bilateral astrocyte responses to unilateral stressors are not unique to glaucoma. After ischemic stroke in the somatosensory cortex, astrocytes within the contralateral area corresponding to the lesion respond to ipsilateral limb stimulation (49), indicating transhemispheric astrocyte crosstalk in another sensory system. Thus, this phenomenon is not unique to the visual system, and studying it could have broad implications on our knowledge of neurodegenerative progression across diseases.

Reactive astrocytes can be derived from complex and heterogeneous populations that vary considerably across spatiotemporal central nervous system networks. Although complex, astrocytes upregulate *Lcn2*/LCN2 both transcriptionally and at the protein level in response to potentially damaging external stimuli, such as bacterial infection/sepsis (26), stroke (25, 32), and neurodegenerative disease (30). These responses have been described across multiple brain regions (28), enabling comparison across regions of interest. As *Lcn2* expression is not observed in physiologically normal astrocytes (or other CNS cells) but is upregulated across reactive subtypes (26, 32), identifying astrocytes that are sensitive to disease conditions is better accomplished with this than with cytoskeletal components like GFAP alone. Indeed, we found that LCN2 was upregulated bilaterally by astrocytes alongside GFAP in response to unilateral IOP elevation, while sham-injected animals exhibited no LCN2 immunoreactivity. This response was pronounced among populations on the surface of the brain and in astrocytes contacting descending vasculature. Astrocytes on the surface form the *glia limitans superficialis* and are a highly specialized subpopulation thought to be early responders to peripheral inflammation (50); astrocytes in contact with vasculature are thought to be similarly specialized (26). These data suggest that a broader program of astrocyte injury response is likely to be upregulated bilaterally upon unilateral insult and that this response may change the way the brain and periphery interact.

Functionally, LCN2 has been linked to antibacterial (51) and anti-inflammatory (52) roles. Increasing the brain's immune function in astrocytes directly contacting the periphery may provide more robust protection against further insult while the degenerating tissue is already in a vulnerable state (15). Further LCN2 functions include facilitating cellular remodeling by increasing the cellular pool of matrix metalloproteinase 9 (MMP9) (53) or even directly destroying extracellular matrix (54). Morphological remodeling in both neurons and astrocytes has been extensively documented in glaucoma models (16, 17, 55, 56). However, LCN2 is a complex protein with many identified functions, and there are contexts in which LCN2 is linked to upregulation of inflammatory pathways (57, 58). Perhaps astrocytes with the most contact with the periphery are primed to quickly respond to peripheral inflammation when the brain is already degenerating and thus more vulnerable to damage (15). The diversity of functional roles for this single protein illustrates the complexity of the astrocyte reactive response and demonstrates why general astrocyte reactivity should not be associated with a purely protective or purely degenerative role. Subtypes of astrocyte reactivity are complex and can occupy multiple functional niches.

Together, these data reveal that local neurodegeneration can initiate a complex, broad, multicellular response throughout multiple brain regions, even early in neurodegenerative progression. By understanding these earliest responses to neurodegenerative stress, we draw closer to earlier diagnoses and provide an opportunity for preventing vision loss through early intervention.

Materials and Methods

Animals. Animal procedures were performed in accordance with the National Institute of Health's guidelines with the approval of NYU School of Medicine's Institutional Animal Care and Use Committee. All animals were housed at 22 to 25 °C with 50 to 60% humidity. Animals had access to food and water ad libitum and were housed on a 12-h light/dark cycle. Mice were C57BL/6J (RRID:IMSR_JAX:000664) with male and female mice equally distributed among experimental conditions.

Intracameral Microbead Injections. Mice were anesthetized with 1-3% isoflurane administered 0.25 to 1 LGP oxygen. Eyes were numbed via 0.5% proparacaine opthalmic drops and dilated via 1% tropicamide opthalmic drops. Micropipettes were pulled from borosilicate glass capillaries, cut to a final diameter of approximately 50 nm, and attached to a microinjector via tubing filled with mineral oil. Micropipettes were mounted to a three-way micromanipulator and backfilled with 2 μL sterile polystyrene microbead solution [Invitrogen FluoSpheres, polystyrene, 15 μm, yellow-green (505/515); Item# F8844]. The micromanipulator was carefully adjusted to insert the cannula into the anterior chamber of an eye stabilized via curved forceps and 0.5 μL microbead solution was injected. Sham mice instead received the same volume of sterile saline. After 20 s, the cannula was removed and antibiotic ophthalmic drops (0.3% ciprofloxacin) were administered. All mice were injected unilaterally; the corresponding contralateral eye remained naïve. Breathing rates and animal behavior following anesthesia were carefully monitored for signs of complications (none detected).

IOP was measured 48 h later via TonoLab rebound tonometer (iCare) and again 3 d later, prior to CTB administration. Mice were transcardially perfused (see below) 7 d following microbead or sham injection.

Intravitreal CTB Injections. Mice were anesthetized with 1 to 3% isoflurane administered 0.25 to 1 LGP oxygen. Eyes were numbed via 0.5% proparacaine opthalmic drops; then, a 34-gauge needle was carefully inserted into the posterior chamber, 1 mm posterior to the superotemporal limbus. 1 μL of CTB conjugated to AlexaFluor-555 was gradually injected; then, antibiotic ophthalmic drops (0.3% ciprofloxacin) were administered. Breathing rates and animal behavior following anesthesia were carefully monitored for signs of complications (none detected).

Tissue Preparation and Initial Clearing. In brief, 7 d following unilateral microbead or sham injection, C57BL/6J mice were heavily anesthetized with an overdose of pentobarbitol (Euthasol: 390 mg Pentobarbital/50 mg Phenytoin/mL at 2 μL/g) and transcardially perfused with PBS containing 10 mg/L Heparin followed by 4% PFA in PBS at RT. Brains were immediately dissected taking care to leave the surface intact and postfixed in 4% PFA in PBS overnight to stabilize tertiary structures of proteins containing glycine residues. Fixed samples were washed in PBS and 0.01% sodium azide three times for 1 h, then stored in PBS/azide until delipidation.

The clearing protocol uses similar principles to the iDISCO+ or AdipoClear protocol (24, 59, 60) with several adjustments specific to brain tissue and this study that facilitate rehydration and restaining. To delipidate, fixed samples were washed in B1N buffer (H_2O/0.1% Triton X-100/0.3 M glycine/0.01% sodium azide, pH 7) for 1 h, followed by 1-h washes each in 20, 40, 60, and 80% methanol in B1N. Samples were fully dehydrated in 100% methanol for three 1-h washes and then delipidated

in 2:1 dichloromethane (DCM; Sigma-Aldrich) overnight. Delipidation resumed the following day in three 1-h washes in 100% DCM. Samples were then washed in 100% methanol for 1 h twice, then rehydrated via 1-h incubations in each 80, 60, 40, and 20% methanol in B1N. Samples were then washed in B1N overnight.

For tissue clearing, samples were dehydrated in a 20, 40, 60, 80, 100, 100, and 100% methanol/H_2O series for 45 min each. Following dehydration, samples were washed in 2:1 DCM:methanol overnight followed by three 1-h washes in 100% DCM. Samples were cleared overnight in dibenzyl ether (DBE, Sigma-Aldrich) and stored at room temperature in the dark in amber glass vials until imaging.

Light Sheet Imaging. Whole, cleared brains were imaged on a light sheet microscope (Zeiss Z1) equipped with 5× objective lenses. Images were collected with two 1,920 × 1,920 pixels sCOMS cameras and acquired using Zen Black software (Zeiss). Samples were staged in a custom imaging chamber filled with DBE and illuminated from both sides by the laser light sheet (light sheet thickness: 4 μm) with a step size of 3.5 μm.

Restaining. Once CTB was initially imaged, brains were rehydrated through three 1-h DCM washes, three 1-h incubations in 100% MeOH, and 1-h washes in each 80, 60, 40, and 20% methanol in B1N; brains were then incubated in B1N overnight. Samples were permeabilized in PTxwH buffer (PBS/0.1% Triton X-100/0.05% Tween 20/2 μg/mL heparin/0.02% sodium azide) with an added 45 g/L glycine and 50 mL/L DMSO two times for 1 h each. Then, samples were washed three times in PTxwH for 1 h.

Samples were incubated in primary antibody (Abcam ab53554; goat anti-GFAP, 1:500 in 5 mL PTxwH) for 1 wk at 37 °C with rotation. After primary incubation, samples were washed in PTxwH with eight solution changes over a period of 3 d, then incubated in Fab-fragment only secondary antibody [Jackson Immuno 705-606-147, F(ab')₂ Donkey-Anti-Goat conjugated to Alexa Fluor 647, 1:800 in 5 mL PTxwH] for 1 wk at 37 °C with rotation. Samples were again washed in PTxwH with eight solution changes over a period of 3 d. Samples were then cleared as above.

CTB Transport Analysis. To assess the CTB transport through the visual tract, raw .zen files were stitched in Zen Blue [Version 3.10] and exported as .tif; those were then converted into .ims via the Imaris File Converter [Version 9.9]. Images were then uploaded into Imaris Bitplane software (Version 10.0) for 3D reconstructions. CTB signal was reconstructed using Imaris' surface tool; individual regions were manually selected within this reconstruction using autofluorescence in an empty 488 channel of each brain prior to analysis (24, 59). For each region or full visual tract, intensity mean, median, and volume were then calculated by Imaris. Each measure was statistically analyzed via one-way ANOVA followed by Tukey's post hoc test when the initial ANOVA rejected the null hypothesis for comparisons among sham-injected optic projections in Fig. 1; when microbead-elevated projections were also assessed, a two-way ANOVA was used instead.

Cleared Brain GFAP Analysis. As in CTB transport analysis, raw .zen files were stitched in Zen Blue [Version 3.10] and exported as .tif; those were then converted into .ims via the Imaris File Converter [Version 9.9]. Images were then uploaded into Imaris Bitplane software (Version 10.0) for 3D reconstructions. Images of CTB signal from the original staining were overlaid onto newly obtained GFAP images and manually aligned using autofluorescence (488) images from each imaging session. Using images obtained in the horizontal plane (as opposed to reconstructions in sagittal or coronal planes), GFAP+ signal was manually outlined; then, the autofluorescence images were used to identify the full brain regions for quantification. CTB signal was reflected and aligned with the autofluorescence images of the opposite hemisphere to identify the CTB+ and CTB− retinotopic complement regions. Once regions were identified, average GFAP intensity within each region was quantified in Imaris then statistically analyzed against corresponding regions via one-way ANOVA followed by Tukey's post hoc test after initial ANOVAs rejected the null hypothesis.

Immunohistochemistry on Floating Sections. Brains were rehydrated as in the Restaining section until the final B1n wash. They were then moved to PBS + 0.01% NaN_3 and sectioned on a vibrating microtome at 100 μm. Floating sections of SC were blocked for 1 h in 5% normal donkey serum (NDS), then incubated overnight in 6% H_2O_2 at 4° with shaking to quench any residual fluorescence; quenching was verified by widefield microscopy. Sections were washed 5 × 10 min in PBS + 0.01% NaN_3, then incubated in primary antibody solution overnight at 4° with shaking [3% NDS, 0.1% Tween-20, 1:250 Rat-anti-GFAP (monoclonal; Life Technologies #130300); 1:500 Rabbit-anti-CTB (polyclonal; Abcam #ab34992)]. Sections were washed 5 × 10 min in PBS + 0.01% NaN_3. To ensure clean staining for quantification, Goat-anti-Mouse-Lipocalin-2 (LCN2; R&D Systems #AF1857) was conjugated to AlexaFluor 647 using Invitrogen's Antibody Labeling Kit (#A20186) following manufacturer's instructions. Sections were then incubated overnight in 1% NDS, 0.1% TritonX-100, 1:500 647-conjugated goat-anti-mouse-LCN2, 1:200 donkey-anti-rat-AlexaFluorPlus555 (Invitrogen #A48270), and 1:200 donkey-anti-rabbit-AlexaFluorPlus488 (Invitrogen #A32790) in PBS + 0.01% NaN_3. Sections were washed 5 × 10 min in PBS + 0.01% NaN_3, then mounted in Fluoromount-G mounting medium (Invitrogen #00-4958-02).

Confocal Imaging and Analysis. Sections were imaged on a Zeiss 800 confocal microscope; montages of full bilateral SCs were obtained using a 20× air objective at 512 × 512 per image, and high-resolution inset images were obtained using a 40× oil objective at 2,048 × 2,048 resolution. Z-stacks were obtained at a step size of 3.12 μm (20×) or 1.37 μm (40×). All sections obtained at the same magnification were imaged using the same settings.

Maximum Z-projections were rendered using FIJI (ImageJ 1.54f), and analysis was performed blinded to sample and condition. ROIs of SC were manually delineated, and mean fluorescence of GFAP and LCN2 was quantified via ImageJ's "Multi Measure" function in the ROI manager. Images were then thresholded uniformly across all samples, and % Area within SC ROIs positive for GFAP or LCN2 fluorescence was again quantified via ImageJ's Multi Measure function in the ROI manager.

Statistics. All statistical analyses were performed in GraphPad Prism 10. When the initial statistical test could reject the null hypothesis, a post hoc test was also implemented as indicated. Exact *P*-values are listed in the figure for each experiment. Sample size for each experiment is indicated in the figure legend for each experiment.

Data, Materials, and Software Availability. All data generated in this study are available on the Brain Image Library database (61).

Author affiliations: ᵃInstitute for Translational Neuroscience, New York University Grossman School of Medicine, New York, NY 10016; ᵇDepartment of Neuroscience, New York University Grossman School of Medicine, New York, NY 10016; ᶜDepartment of Ophthalmology, New York University Langone Health, New York, NY 10016; and ᵈDepartment of Psychiatry, New York University Langone Health, New York, NY 10016

1. Y. C. Tham *et al.*, Global prevalence of glaucoma and projections of glaucoma burden through 2040: A systematic review and meta-analysis. *Ophthalmology* **121**, 2081–2090 (2014).
2. A. Karimi *et al.*, Morphological and biomechanical analyses of the human healthy and glaucomatous aqueous outflow pathway: Imaging-to-modeling. *Comput. Methods Progr. Biomed.* **236**, 107485 (2023).
3. A. Vahabikashi *et al.*, Increased stiffness and flow resistance of the inner wall of Schlemm's canal in glaucomatous human eyes. *Proc. Natl. Acad. Sci. U.S.A.* **116**, 26555–26563 (2019).
4. J. D. Stein, A. P. Khawaja, J. S. Weizer, Glaucoma in adults-screening, diagnosis, and management: A review. *JAMA* **325**, 164–174 (2021).
5. R. N. Weinreb *et al.*, Risk assessment in the management of patients with ocular hypertension. *Am. J. Ophthalmol.* **138**, 458–467 (2004).
6. H. R. Yum, H. L. Park, C. K. Park, Characteristics of normal-tension glaucoma patients with temporal retinal nerve fibre defects. *Sci. Rep.* **10**, 6362 (2020).
7. M. A. Margeta *et al.*, Apolipoprotein E4 impairs the response of neurodegenerative retinal microglia and prevents neuronal loss in glaucoma. *Immunity* **55**, 1627–1644.e1627 (2022).
8. C. Crump, J. Sundquist, W. Sieh, K. Sundquist, Risk of Alzheimer's disease and related dementias in persons with glaucoma: A national cohort study. *Ophthalmology* **131**, 302–309 (2024).

9. J. D. Ho, C. C. Hu, H. C. Lin, Open-angle glaucoma and the risk of stroke development: A 5-year population-based follow-up study. *Stroke* **40**, 2685–2690 (2009).
10. H. C. Lin, C. W. Chien, C. C. Hu, J. D. Ho, Comparison of comorbid conditions between open-angle glaucoma patients and a control cohort: A case–control study. *Ophthalmology* **117**, 2088–2095 (2010).
11. P. A. Williams *et al.*, Vitamin B(3) modulates mitochondrial vulnerability and prevents glaucoma in aged mice. *Science* **355**, 756–760 (2017).
12. S. D. Crish, R. M. Sappington, D. M. Inman, P. J. Horner, D. J. Calkins, Distal axonopathy with structural persistence in glaucomatous neurodegeneration. *Proc. Natl. Acad. Sci. U.S.A.* **107**, 5196–5201 (2010).
13. S. H. Shah, J. L. Goldberg, The role of axon transport in neuroprotection and regeneration. *Dev. Neurobiol.* **78**, 998–1010 (2018).
14. M. L. Cooper, D. J. Calkins, Beyond hypertrophy: Changing views of astrocytes in glaucoma. *Vision Res.* **223**, 108461 (2024).
15. M. L. Cooper *et al.*, Redistribution of metabolic resources through astrocyte networks mitigates neurodegenerative stress. *Proc. Natl. Acad. Sci. U.S.A.* **117**, 18810–18821 (2020).
16. M. L. Cooper, J. W. Collyer, D. J. Calkins, Astrocyte remodeling without gliosis precedes optic nerve axonopathy. *Acta Neuropathol. Commun.* **6**, 38 (2018).
17. M. L. Cooper, S. D. Crish, D. M. Inman, P. J. Horner, D. J. Calkins, Early astrocyte redistribution in the optic nerve precedes axonopathy in the DBA/2J mouse model of glaucoma. *Exp. Eye Res.* **150**, 22–33 (2016).
18. Y. Takihara *et al.*, In vivo imaging of axonal transport of mitochondria in the diseased and aged mammalian CNS. *Proc. Natl. Acad. Sci. U.S.A.* **112**, 10515–10520 (2015).
19. S. H. Shah *et al.*, Quantitative transportomics identifies Kif5a as a major regulator of neurodegeneration. *eLife* **11**, e68148 (2022).
20. J. A. Wurl, C. E. Mac Nair, J. A. Dietz, V. I. Shestopalov, R. W. Nickells, Contralateral astrocyte response to acute optic nerve damage is mitigated by PANX1 channel activity. *Int. J. Mol. Sci.* **24**, 15641 (2023).
21. A. Kanamori, M. Nakamura, Y. Nakanishi, Y. Yamada, A. Negi, Long-term glial reactivity in rat retinas ipsilateral and contralateral to experimental glaucoma. *Exp. Eye Res.* **81**, 48–56 (2005).
22. B. I. Gallego *et al.*, IOP induces upregulation of GFAP and MHC-II and microglia reactivity in mice retina contralateral to experimental glaucoma. *J. Neuroinflammation* **9**, 92 (2012).
23. P. Chaudhary *et al.*, Optic nerve head myelin-related protein, GFAP, and Iba1 alterations in non-human primates with early to moderate experimental glaucoma. *Invest. Ophthalmol. Vis. Sci.* **63**, 9 (2022).
24. N. Renier *et al.*, iDISCO: A simple, rapid method to immunolabel large tissue samples for volume imaging. *Cell* **159**, 896–910 (2014).
25. J. L. Zamanian *et al.*, Genomic analysis of reactive astrogliosis. *J. Neurosci.* **32**, 6391–6410 (2012).
26. P. Hasel, I. V. L. Rose, J. S. Sadick, R. D. Kim, S. A. Liddelow, Neuroinflammatory astrocyte subtypes in the mouse brain. *Nat. Neurosci.* **24**, 1475–1487 (2021).
27. Y. M. Park, H. Chun, J. I. Shin, C. J. Lee, Astrocyte specificity and coverage of hGFAP-CreERT2 [Tg(GFAP-Cre/ERT2)13Kdmc] mouse line in various brain regions. *Exp. Neurobiol.* **27**, 508–525 (2018).
28. F. Endo *et al.*, Molecular basis of astrocyte diversity and morphology across the CNS in health and disease. *Science* **378**, eadc9020 (2022).
29. Z. Jiwaji *et al.*, Reactive astrocytes acquire neuroprotective as well as deleterious signatures in response to Tau and Aß pathology. *Nat. Commun.* **13**, 135 (2022).
30. R. Patani, G. E. Hardingham, S. A. Liddelow, Functional roles of reactive astrocytes in neuroinflammation and neurodegeneration. *Nat. Rev. Neurol.* **19**, 395–409 (2023).
31. S. A. Liddelow *et al.*, Neurotoxic reactive astrocytes are induced by activated microglia. *Nature* **541**, 481–487 (2017).
32. R. D. Kim *et al.*, Temporal and spatial analysis of astrocytes following stroke identifies novel drivers of reactivity. bioRxiv [Preprint] (2023). https://doi.org/10.1101/2023.11.12.566710 (Accessed 2 February 2024).
33. E. M. Martersteck *et al.*, Diverse central projection patterns of retinal ganglion cells. *Cell Rep.* **18**, 2058–2072 (2017).
34. L. Della Santina, D. M. Inman, C. B. Lupien, P. J. Horner, R. O. Wong, Differential progression of structural and functional alterations in distinct retinal ganglion cell types in a mouse model of glaucoma. *J. Neurosci.* **33**, 17444–17457 (2013).
35. Z. Tan *et al.*, Microglia depletion exacerbates retinal ganglion cell loss in a mouse model of glaucoma. *Exp. Eye Res.* **225**, 109273 (2022).
36. Y. Ou, R. E. Jo, E. M. Ullian, R. O. Wong, L. Della Santina, Selective vulnerability of specific retinal ganglion cell types and synapses after transient ocular hypertension. *J. Neurosci.* **36**, 9240–9252 (2016).
37. M. Solino, A. Yu, L. Della Santina, Y. Ou, Large-scale survey of excitatory synapses reveals sublamina-specific and asymmetric synapse disassembly in a neurodegenerative circuit. *iScience* **26**, 107262 (2023).
38. A. W. Kong *et al.*, Asymmetric functional impairment of ON and OFF retinal pathways in glaucoma. *Ophthalmol. Sci.* **1**, 100026 (2021).
39. R. A. Giolli, R. H. Blanks, F. Lui, The accessory optic system: Basic organization with an update on connectivity, neurochemistry, and function. *Prog. Brain Res.* **151**, 407–440 (2006).
40. K. B. VanderWall *et al.*, Differential susceptibility of retinal ganglion cell subtypes in acute and chronic models of injury and disease. *Sci. Rep.* **10**, 17359 (2020).
41. S. Daniel, A. F. Clark, C. M. McDowell, Subtype-specific response of retinal ganglion cells to optic nerve crush. *Cell Death Discov.* **4**, 7 (2018).
42. S. Daniel, K. J. Meyer, A. F. Clark, M. G. Anderson, C. M. McDowell, Effect of ocular hypertension on the pattern of retinal ganglion cell subtype loss in a mouse model of early-onset glaucoma. *Exp. Eye Res.* **185**, 107703 (2019).
43. A. Y. M. Wang *et al.*, An ON-type direction-selective ganglion cell in primate retina. *Nature* **623**, 381–386 (2023).
44. T. Baden *et al.*, The functional diversity of retinal ganglion cells in the mouse. *Nature* **529**, 345–350 (2016).
45. W. F. Hoyt, O. Luis, The primate chiasm. Details of visual fiber organization studied by silver impregnation techniques. *Arch. Ophthalmol.* **70**, 69–85 (1963).
46. F. Briggs, W. M. Usrey, Corticogeniculate feedback and visual processing in the primate. *J. Physiol.* **589**, 33–40 (2011).
47. V. Murcia-Belmonte *et al.*, A retino-retinal projection guided by Unc5c emerged in species with retinal waves. *Curr. Biol.* **29**, 1149–1160.e1144 (2019).
48. M. A. Reilly, A. Villarreal, T. Maddess, W. E. Sponsel, Refined frequency doubling perimetry analysis reaffirms central nervous system control of chronic glaucomatous neurodegeneration. *Transl. Vis. Sci. Technol.* **4**, 7 (2015).
49. Y. Takatsuru *et al.*, Critical role of the astrocyte for functional remodeling in contralateral hemisphere of somatosensory cortex after stroke. *J. Neurosci.* **33**, 4683–4692 (2013).
50. P. Hasel *et al.*, Defining the molecular identity and morphology of glia limitans superficialis astrocytes in mouse and human. bioRxiv [Preprint] (2023). https://doi.org/10.1101/2023.04.06.535893 (Accessed 6 March 2024).
51. M. Nairz *et al.*, Absence of functional Hfe protects mice from invasive *Salmonella enterica* serovar Typhimurium infection via induction of lipocalin-2. *Blood* **114**, 3642–3651 (2009).
52. H. Du *et al.*, Lipocalin-2 alleviates LPS-induced inflammation through alteration of macrophage properties. *J. Inflamm. Res.* **14**, 4189–4203 (2021).
53. H. Kobara *et al.*, Lipocalin2 enhances the matrix metalloproteinase-9 activity and invasion of extravillous trophoblasts under hypoxia. *Placenta* **34**, 1036–1043 (2013).
54. S. A. Jaberi *et al.*, Lipocalin-2: Structure, function, distribution and role in metabolic disorders. *Biomed. Pharmacother.* **142**, 112002 (2021).
55. D. Sun, J. Qu, T. C. Jakobs, Reversible reactivity by optic nerve astrocytes. *Glia* **61**, 1218–1235 (2013).
56. S. Tehrani, E. C. Johnson, W. O. Cepurna, J. C. Morrison, Astrocyte processes label for filamentous actin and reorient early within the optic nerve head in a rat glaucoma model. *Invest. Ophthalmol. Vis. Sci.* **55**, 6945–6952 (2014).
57. S. Lee *et al.*, Lipocalin-2 is an autocrine mediator of reactive astrocytosis. *J. Neurosci.* **29**, 234–249 (2009).
58. R. Liu *et al.*, NOX activation in reactive astrocytes regulates astrocytic LCN2 expression and neurodegeneration. *Cell Death Dis.* **13**, 371 (2022).
59. J. Chi, A. Crane, Z. Wu, P. Cohen, Adipo-clear: A tissue clearing method for three-dimensional imaging of adipose tissue. *J. Vis. Exp.* **137**, 58271 (2018), 10.3791/58271.
60. A. Branch *et al.*, An optimized tissue clearing protocol for rat brain labeling, imaging, and high throughput analysis. bioRxiv [Preprint] (2021). https://doi.org/10.1101/639674 (Accessed 9 July 2023).
61. M. L. Cooper, H. K. Gildea, M. C. Selles, S. A. Liddelow, M. V. Chao, Astrocytes in the mouse brain respond bilaterally to unilateral retinal neurodegeneration. Brain Image Library. https://doi.org/10.35077/g.1170. Deposited 21 February 2025.